

Coarse-to-Fine Domain Incremental Learning with Attentive Distillation for Mining Footprint Segmentation in Multispectral Imagery

Alif Tri Handoyo^{1*}, Vincent C.S. Lee², Rizka Widyarini Purwanto¹, Alex M. Lechner^{1,3}, Deanna Kemp⁴ and Muhamad Risqi U. Saputra^{1*}

¹Monash University, Indonesia

²Monash University, Australia

³Northeastern University, China

⁴The University of Queensland, Australia

{alif.handoyo, vincent.cs.lee, rizka.purwanto, alex.lechner}@monash.edu, d.kemp@uq.edu.au, risqi.saputra@monash.edu

Abstract

Automatically mapping and segmenting global mining footprints using remote sensing and deep learning is critical for monitoring the socio-environmental risks and impacts of mining, yet its progress is hindered by the scarcity of fine-grained annotated data. Although large-scale datasets with coarse boundaries are widely available, leveraging them to improve fine-grained segmentation is challenging due to significant domain shift. To address this, we propose MineC2FNet, a coarse-to-fine domain incremental learning framework that exploits abundant coarse data to enhance fine-grained mining footprint segmentation. MineC2FNet adopts a teacher–student architecture with attentive distillation at both the feature and prediction levels, selectively transferring generalized knowledge from the coarse domain while enabling boundary refinement using limited fine-grained data (fine domain). We further introduce an expertly validated dataset of 219 images with precise boundary annotations across diverse geographies and commodities. Extensive experiments against state-of-the-art approaches, including domain adaptation and domain incremental learning methods, demonstrate that MineC2FNet achieves superior performance while effectively handling domain shift. The dataset and code are publicly available at <https://github.com/risqiutama/MineC2FNet>.

1 Introduction

Mapping Global Mining Footprints: A Socio-Environmental Monitoring Challenge. Mining is fundamental to the global economy, yet mineral resource extraction can cause profound, often irreversible damage to people and the environment [Owen *et al.*, 2023].

Extractive activities can lead to large-scale landscape alteration, ecosystem loss, biodiversity decline, and air and water

pollution [Sontner *et al.*, 2018; Lechner *et al.*, 2017]. Many of these impacts can displace local and downstream populations and adversely affect the health of local communities and indigenous peoples [Ang *et al.*, 2023; Owen *et al.*, 2023]. These pressures and impacts can also drive resource-related conflicts and grievances.

Despite the promise of local economic development, host communities often live with long-term environmental legacies, long after mines cease operations [Kemp and Owen, 2025]. Multispectral remote sensing offers a method for continuous and repeatable tracking of mining footprints, in particular in remote areas [Lechner *et al.*, 2019; Maus *et al.*, 2020; Saputra *et al.*, 2025]. This would enable scalable, remote monitoring of mining activity and its surrounding context, including how mining footprints change over time, and where change coincides with complex social and environmental risk factors.

However, a critical bottleneck remains: while Deep Learning (DL)-based semantic segmentation offers a transformative alternative to labor-intensive manual mapping [Wieland *et al.*, 2023; Cai *et al.*, 2023; Zhu *et al.*, 2025], these models depend on vast amounts of meticulously annotated data. Generating such data is exceptionally challenging, as distinguishing fine-grained features (e.g., pits, waste rock, tailings dams) requires substantial expert knowledge and field surveys [Maus *et al.*, 2020]. Although coarsely annotated data [Maus *et al.*, 2022] offers a cost-effective alternative with extensive coverage, it merges distinct land cover features into imprecise footprints (Figure 1 (a) - Task 1). Models trained on such labels inherit these imprecisions, leading to inaccurate boundary delineation and hindering effective environmental monitoring.

Our Contribution. To leverage both abundant coarse dataset and scarce fine dataset for mining footprint segmentation, and to bridge their domain gap in incremental learning settings, we propose Mine Coarse-to-Fine Net (MineC2FNet). MineC2FNet uses *attentive distillation* in a teacher–student training settings to adapt the model to new domains while selectively retaining knowledge from previous domains. The attentive distillation is applied at both feature (via *attentive feature injection*) and prediction levels (via *at-*

*Corresponding authors.

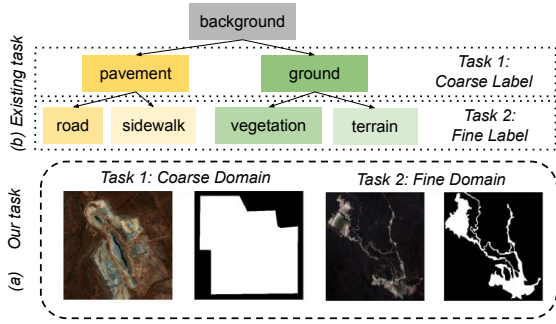


Figure 1: Comparison between (a) our coarse-to-fine problem with (b) existing coarse-to-fine continual learning task.

tentive knowledge transfer) to transfer only high-quality delineation from the teacher (previous domain) to the student (new domain). Unlike prior coarse-to-fine continual learning methods defining "coarse" as broad label categories [Shenaj *et al.*, 2022; Alfarrar *et al.*, 2024], we introduce a new task where "coarse" refers to imprecise boundaries and "fine" to accurate, expert-validated ones. The contributions of this paper are:

- We present MineC2FNet, the first coarse-to-fine domain incremental learning framework for mining footprint segmentation using multispectral imagery.
- We propose attentive distillation, a novel approach applying selective distillation to both feature and prediction levels.
- We introduce a new, expertly validated dataset of 219 globally distributed images for fine-grained mining footprint segmentation.
- We demonstrate the effectiveness of our framework and attentive distillation through comprehensive evaluation on this new dataset.

Team. Our project brought together a multidisciplinary team in remote sensing, deep learning, and mining domain experts, including professionals from the Faculty of IT at Monash University, the College of Resources and Civil Engineering at Northeastern University, China, and the Centre for Social Responsibility in Mining at the University of Queensland. These experts were key to guiding the project conceptualisation, identifying detailed mining features, and validating the quality of our new dataset. More broadly, funded by the Ford Foundation, our research contributes to the foundations mission of advancing social and environmental justice by improving transparency and accountability in mining.

2 Related Works

Semantic Segmentation of Mining Footprint. Applying deep learning-based semantic segmentation to multispectral satellite imagery has the potential to transform global mining footprint mapping and monitoring. Currently, global-scale studies, e.g., [Owen *et al.*, 2023], rely on a single geographic coordinate to represent mining operations, failing to capture their true spatial extent. On the other hand, studies

that leverage supervised semantic segmentation are typically mine- or region-specific [Qiao *et al.*, 2024; Tong *et al.*, 2020], restricting their application to global datasets. Although [Saputra *et al.*, 2025] has demonstrated mining segmentation on a global dataset, their model was trained on only 37 locations, limiting its generalization capability. Finally, the success of these methods is fundamentally dependent on the availability of large-scale, pixel-level annotated datasets, which are unfortunately not yet available.

Continual Learning in Remote Sensing. Continual Learning (CL) addresses the challenge of training a model on a continuous stream of data or a sequence of tasks without experiencing *catastrophic forgetting*, a condition in which the model tends to lose previously learned knowledge when trained on a new dataset or tasks.

In remote sensing, the coarse-to-fine paradigm is applied to address CL problems in several distinct ways, ranging from data quality to architectural precision. To mitigate the problem of high annotation costs, some frameworks leverage coarse labels as a starting point to automatically generate more detailed, fine-grained pseudo-labels. These new pseudo labels then serve as the actual supervision to train the model. This strategy can be applied spatially, by turning imprecise polygons into sharp object boundaries [Das *et al.*, 2023], or semantically, by using coarse labels (broad classes, e.g., cropland) to identify and classify fine labels (specific sub-classes, e.g., paddy field) [Chen *et al.*, 2024]. Similarly, [Shenaj *et al.*, 2022] facilitates this coarse-to-fine CL by using knowledge distillation and a specialized weight initialization rule, allowing the model to learn new classes and adapt to new domains without being fully retrained.

Beyond class-incremental shifts, domain-incremental learning (DIL) tackles geographical variations by adapting the models to new spectral and spatial distributions without requiring access to original training data. The GSMF-RS-DIL [Huang *et al.*, 2024] framework utilizes graph space transformations and multifeature constraints to balance prior knowledge retention with the acquisition of new domain information. Similarly, multi-domain incremental architectures [Garg *et al.*, 2022] employ domain-specific parameters and differential learning rates within Domain-Aware Residual Units to optimize the stability-plasticity trade-off. These integrated strategies allow remote sensing models to remain effective across diverse environments while significantly mitigating catastrophic forgetting.

3 Data

Coarse Dataset. The coarse dataset was derived from the global-scale mining polygons (Version 2) data introduced by [Maus *et al.*, 2022], which originally contained over 44,929 mining polygons. This dataset provides a broader set of image features for mine footprint identification, characterized by rough, less precise edge delineations. These polygons are labeled as "Mining" and areas outside the polygons are considered "Non-Mining", resulting in a binary segmentation. To create a usable subset for our training, we filtered these polygons by establishing a minimum area threshold of approximately 9.8 km², corresponding to the smallest mine in

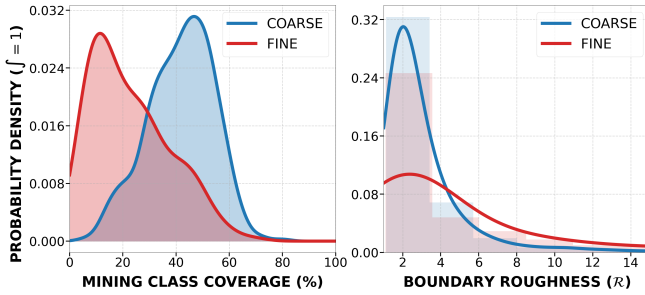


Figure 2: Domain shift analysis using Kernel Density Estimation (KDE). (Left) The coarse dataset exhibits a balanced class distribution, in contrast to the severe class imbalance of the fine dataset. (Right) Boundary roughness analysis demonstrating higher geometric complexity of fine masks compared to coarse masks.

our fine-grained dataset. Polygons with an area greater than this threshold were retained, resulting in a collection of 1,380 coarse-labeled images. Satellite imagery for these locations were sourced from Sentinel-2 (10m) and Landsat 8 (15/30m) satellites and included RGB, Near-Infrared (NIR), and Short-Wave Infrared (SWIR) bands.

Fine Dataset. The fine dataset is a high-quality, expert-validated collection of images featuring precise and detailed boundaries for mining segmentation. This dataset consists of 219 images, which include RGB and NIR bands, with a subset of 200 images also containing SWIR bands. These data were manually harmonised from the original datasets of [Werner *et al.*, 2020; Lechner *et al.*, 2016; Lechner *et al.*, 2019], following methods outlined in [Saputra *et al.*, 2025]. Similar to the coarse dataset, the resolution and extent of the multispectral data varied as we used Sentinel and Landsat 8. We split the dataset into training, validation, and test sets using an approximate 70:10:20 ratio. These locations was carefully balanced to account for a wide range of mine commodities, geographic regions, and climates. A key characteristic is its significant class imbalance, with non-mining pixels making up more than 80% of the labels across the dataset.

Domain Shift. Figure 2 demonstrates a clear domain gap between the coarse and fine datasets. The mining class coverage analysis (left) reveals a significant disparity in class labels pixel distributions: Coarse annotations exhibit a relatively balanced occupancy peaking at 45%, whereas the fine dataset reflects the extreme sparsity of precise footprints, peaking at only 12%. The Boundary Roughness (right) measured as $\mathcal{R} = \frac{P^2}{4\pi A}$ further differentiates the masks roughness. Coarse masks peak at $\mathcal{R} \approx 2$, identifying them as smooth, simplified blobs. In contrast, fine labels capture the irregular, high-frequency boundary details of real-world mines, with values reaching up to $\mathcal{R} \approx 12$. Collectively, these metrics confirm that while coarse labels provide a simplified approximation, fine labels capture the true geometric complexity and natural class imbalance inherent in the target domain.

4 Methodology

Our proposed method addresses the domain shift between coarse and fine datasets in training domain incremental learn-

ing model for mining footprint segmentation using multispectral satellite imagery. Figure 3 illustrates the overall workflow, highlighting our framework with attentive distillation applied at both the feature level (via Attentive Feature Injection) and the prediction level (via Attentive Knowledge Transfer). The core objective is to enable the model to learn from the new domain while selectively retaining knowledge from the previous domain.

4.1 Problem Formulation

We frame our coarse-to-fine segmentation problem as a domain incremental learning problem consisting of two sequential tasks. The goal is to train a model M , parameterized by θ , that leverages knowledge from an initial task trained on coarse domain D_c , to excel at a subsequent task with fine target domain D_f . This requires a domain incremental learning approach with selective attentive distillation, where the model is capable of transferring relevant general knowledge while discarding domain-specific noise (e.g., imprecise boundaries) from the coarse task.

Let $D_c = \{(X_i^c, Y_i^c)\}_{i=1}^{N_c}$ be the coarsely annotated dataset where X_i^c is an input image, Y_i^c is its corresponding coarse segmentation mask or label, and N_c is the number of coarse training images. Let $D_f = \{(X_i^f, Y_i^f)\}_{i=1}^{N_f}$ be the fine-grained, expertly annotated dataset, where Y_i^f is the precise, fine-grained mask, and N_f is the total images in the fine dataset. Our model, $M(\theta)$, which consists of a teacher component $M(\theta_T)$ and a student component $M(\theta_S)$, where $\theta = \{\theta_T, \theta_S\}$, will be trained using the following steps:

1. **Task 1 (Coarse Domain):** The teacher model $M(\theta_T)$ is trained on the coarse dataset D_c to learn a set of generalized parameters θ_T .
2. **Task 2 (Fine Domain):** With the teacher $M(\theta_T)$ frozen, the student model $M(\theta_S)$ is trained on the fine dataset D_f to learn its parameters θ_S . During this phase, the student must learn to predict the fine labels Y_f while selectively distilling knowledge from $M(\theta_T)$.

The final objective is to optimize the parameters θ_S as described in Equation 1, where L is the loss function.

$$M(\theta_S) = \arg \min_{\theta_S} L(\theta_S | D_f, M(\theta_T)) \quad (1)$$

4.2 Coarse-to-fine Domain Incremental Learning

In the context of our coarse-to-fine domain incremental learning, the training for Task 1 follows the standard training procedure for semantic segmentation, utilizing Binary Cross-Entropy (BCE) [Mao *et al.*, 2023] as the loss function. On the other hand, the training process for Task 2 is orchestrated by a composite loss function, L_{total} . This loss, shown in Eq. (2), is the core of our domain incremental learning approach. It combines L_{student} , the student’s loss function on the fine data, with L_{distill} , the attentive distillation loss from the teacher.

$$L_{\text{total}}(D_f) = L_{\text{student}} + L_{\text{distill}} \quad (2)$$

Student Loss. The student loss, L_{student} , is a comprehensive objective function designed to train the student model $M(\theta_S)$ on the fine-grained dataset D_f . As seen in Eq. (3), it

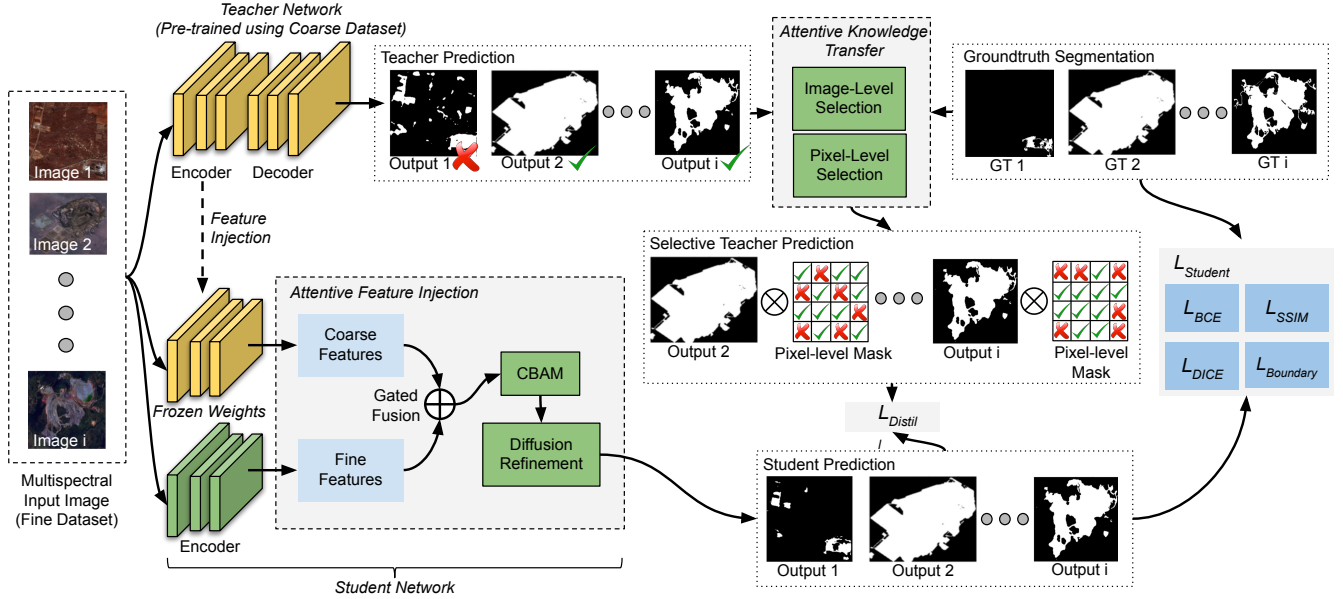


Figure 3: Overview of our coarse-to-fine domain incremental learning framework for mining footprint segmentation (MineC2FNet).

consists of four components, including Binary Cross-Entropy (L_{BCE}), Dice Loss (L_{Dice}), Structural Similarity Loss (L_{SSIM}), and Boundary Loss ($L_{Boundary}$) functions.

$$L_{student}(D_f) = L_{BCE} + L_{Dice} + L_{SSIM} + L_{Boundary} \quad (3)$$

L_{BCE} is utilized as a widely used loss function for binary classification tasks, which we apply on a pixel-wise basis to measure the difference between the student's prediction \hat{Y}_i^f and the ground truth fine mask Y_i^f . The Dice loss is added since it is particularly effective for segmentation tasks with imbalanced classes by maximizing the overlap between \hat{Y}_i^f and Y_i^f [Sudre *et al.*, 2017]. Furthermore, we also incorporate L_{SSIM} [Zhao *et al.*, 2019] as this loss encourages the model to preserve the structural information of Y_i^f , which is crucial for maintaining realistic mining shapes.

Besides the loss functions above, we also incorporate $L_{Boundary}$ to explicitly improve the model performance on edge delineation. This loss is designed by generating a boundary importance map from the ground truth mask and then using it to weight the L_{BCE} . In particular, we first apply Sobel filters to Y_i^f to compute the horizontal (G_x) and vertical (G_y) gradients. The boundary importance map $\hat{W} \in [0, 1]$ is then calculated as in Eq. (4).

$$\hat{W} = \frac{W - W_{\min}}{W_{\max} - W_{\min}}, \text{ where } W = \sqrt{G_x^2 + G_y^2} \quad (4)$$

$L_{Boundary}$ is then defined as a weighted binary-cross entropy loss as described in Eq. (5), where the weights are derived from image edges to emphasize optimizing the boundary regions of the segmented images.

$$L_{Boundary} = \frac{1}{K} \sum_{j=1}^K \hat{W}_j \cdot L_{BCE_j} \quad (5)$$

Note that K represents the number of pixel in the images. This formulation forces the model to pay more attention to correctly classifying pixels on the segmented boundaries.

Distillation Loss. We adopt a knowledge distillation where the loss ($L_{Distill}$) is formulated as the standard Kullback-Leibler (KL) divergence between the softened probability distributions of the teacher (P^T) and student (Q^T), scaled by a temperature factor T . As the teacher is trained in a domain with imperfect coarse labels, we introduce attentive distillation to ensure only reliable knowledge is transferred. This mechanism is applied at both the feature and prediction levels, as we will detail next.

4.3 Attentive Feature Injection

Our attentive feature injection is a multi-stage pipeline designed to intelligently transfer generalized feature extraction capabilities of the teacher model $M(\theta_T)$ to the student $M(\theta_S)$. This pipeline was designed to solve our domain incremental challenge with the understanding that $M(\theta_T)$ was trained on a larger set (source domain), capturing a more visually diverse range of global mining footprints. As a result, $M(\theta_T)$ possesses generalized knowledge of how mining areas appear in satellite imagery, even though its boundary delineation remains imprecise. To this end, rather than simply fine-tuning $M(\theta_T)$'s weight in the Task 2 or even concatenating $M(\theta_T)$'s and $M(\theta_S)$'s features, our attentive feature injection selectively fuses, refines, and enhances feature maps from both the teacher (generalized source domain features that uses coarse data) and student (specific target domain features that uses fine data). As illustrated in Figure 3, the pipeline consists of four stages: Feature Injection, Gated Fusion (GF), Convolutional Block Attention Module (CBAM), and Diffusion Refinement (DR).

Feature Injection. A key distinction in our attentive distillation approach is that we inject a subset of $M(\theta_T)$, particularly the feature extractor, to $M(\theta_S)$, enabling $M(\theta_S)$ to incorporate dual, identical feature extractors: a "teacher feature extractor" (a frozen copy of the teacher's backbone, part of θ_T) and a "student feature extractor" (with trainable parameters, part of θ_S). During Task 2, for a given input image X_i^f , these two backbones operate in parallel. The student backbone extracts high-fidelity features directly from the fine-grained target domain input, while the frozen teacher backbone provides a parallel stream of generalized feature maps derived from the source domain. These two sets of features, one rich in precise target domain detail (F_{fine}) and the other in broad source domain context (F_{coarse}), are then passed to the subsequent attentive fusion and refinement stages.

Gated Fusion (GF). To dynamically merge contextual information from the coarse teacher backbone with high-frequency details from the fine student backbone, we employ Gated Fusion [Takikawa *et al.*, 2019]. This module's merit lies in its learnable, pixel-wise gating mechanism, which adaptively decides the contribution of each feature source. This allows the network to prioritize general context or precise detail as needed, creating a richer, fused representation without the need for fixed fusion rules.

CBAM. The fused features are then refined using the Convolutional Block Attention Module [Woo *et al.*, 2018]. We use CBAM for its efficiency and effectiveness in feature enhancement. Its primary benefit is that it sequentially infers attention maps along both channel and spatial dimensions. This process allows the model to learn what features are most salient (channel-wise) and where to focus its attention (spatial-wise), further boosting the discriminative power of the representations.

Diffusion Refinement (DR). As a final stage, we introduce a new Diffusion Refinement module to produce a highly polished representation for segmentation. Inspired by iterative refinement frameworks [Lin *et al.*, 2017a], our module progressively enhances features by propagating information through a sequence of custom refinement blocks. The key idea of our design is the structure of each block, which combines a convolution, a CBAM layer, and a residual connection to effectively sharpen noisy features. For each refinement step $t \in [1, T]$, the feature map F_{t-1} is updated using the operations detailed in Eq. (6)-(8).

$$F_{\text{conv}_t} = \text{Conv}_{3 \times 3}(F_{t-1}) \quad (6)$$

$$F_{\text{att}_t} = \text{CBAM}(F_{\text{conv}_t}) \quad (7)$$

$$F_t = F_{\text{att}_t} + F_{t-1} \quad (8)$$

This iterative process results in a final feature map, F_{refined} , with an enhanced focus on the most salient regions and channels, making it highly effective for achieving accurate semantic segmentation.

4.4 Attentive Knowledge Transfer

In addition to attentive feature injection, we introduce an attentive knowledge transfer mechanism at the prediction level. A key challenge is that a standard teacher trained

on the coarse domain is not infallible; unconditional (non-selective) distillation transfers domain-specific noise like imprecise boundaries, degrading performance. To mitigate this, our framework adaptively selects *when* and *where* to apply the distillation loss, ensuring that the student only learns from the teacher's most confident and accurate predictions.

Image-level Selection. The first layer of our attentive mechanism operates at the image level, aiming to identify images within a training batch where the teacher model $M(\theta_T)$ produces more accurate predictions than the student model $M(\theta_S)$. This is based on the hypothesis that distillation is beneficial only when $M(\theta_T)$ is more accurate than $M(\theta_S)$ for a given input image. We formalize this by utilizing an indicator function $\mathbb{I}(\cdot)^{\text{img}}$ which returns 1 if $L_{\text{BCE}}(Y_i^f, P_i) < L_{\text{BCE}}(Y_i^f, Q_i)$ and 0 otherwise. Note that P_i and Q_i denote the output prediction (logits) of $M(\theta_T)$ and $M(\theta_S)$, respectively, for image i . The distillation loss with image-level selection is then formulated in Eq. (9).

$$L_{\text{distill}}^{\text{image}} = \frac{T^2}{N_f} \sum_{i=1}^{N_f} \mathbb{I} \left(\begin{array}{l} L_{\text{BCE}}(Y_i^f, P_i) \\ < L_{\text{BCE}}(Y_i^f, Q_i) \end{array} \right)^{\text{img}} \cdot \text{KL}(P_i^T \parallel Q_i^T) \quad (9)$$

Pixel-level Selection. The second layer of attentive distillation applies at the pixel level. In the context of semantic segmentation, as L_{distill} will be computed for every single pixel, we realize that not all per-pixel teacher's prediction will be accurate, especially when the teacher was trained using imprecise ground truth labels. To this end, we selectively apply distillation only when the teacher's prediction at the pixel level is more accurate than the student's prediction. Similar to image-level selection, we formalize this pixel-level selection by utilizing an indicator function $\mathbb{I}(\cdot)^{\text{pxl}}$ which returns 1 if $L_{\text{BCE}}(Y_{ij}^f, P_{ij}) < L_{\text{BCE}}(Y_{ij}^f, Q_{ij})$ and 0 otherwise. Note that $j \in K$ represents the pixel index in image i . The distillation loss with pixel-level selection is formulated in Equation 10.

$$L_{\text{distill}}^{\text{pixel}} = \frac{T^2}{N_f} \sum_{i,j} \mathbb{I} \left(\begin{array}{l} L_{\text{BCE}}(Y_{ij}^f, P_{ij}) \\ < L_{\text{BCE}}(Y_{ij}^f, Q_{ij}) \end{array} \right)^{\text{pxl}} \cdot \text{KL}(P_{ij}^T \parallel Q_{ij}^T) \quad (10)$$

Note that in practice, \mathbb{I}^{pxl} will be in a matrix form rather than in a scalar form as in \mathbb{I}^{img} .

Hybrid Selection. Our final approach combines both image-level and pixel-level selection strategies into a hybrid selection mask $\mathbb{I}^{\text{hybrid}}$ by performing element-wise multiplication of \mathbb{I}^{pxl} and \mathbb{I}^{img} as shown in Eq. (11).

$$\mathbb{I}_{ij}^{\text{hybrid}} = \mathbb{I}_i^{\text{img}} \cdot \mathbb{I}_{ij}^{\text{pxl}} \quad (11)$$

This ensures that distillation is applied only to pixels where the teacher is more accurate than the student, and only within input images where the teacher demonstrates overall superior performance. The final distillation loss is computed as defined in Eq. (12):

$$L_{\text{distill}} = \frac{\sum_{i,j} \left(\mathbb{I}_{ij}^{\text{hybrid}} \cdot T^2 \cdot \text{KL}(P_{ij}^T \parallel Q_{ij}^T) \right)}{\sum_{i,j} \mathbb{I}_{ij}^{\text{hybrid}} + \epsilon} \quad (12)$$

Model	Acc.	mF1	mIoU
CNN and Transformer-based methods (Transfer Learning)			
U-Net [Ronneberger <i>et al.</i> , 2015]	89.79	79.52	67.26
DeepLabV3+ [Chen <i>et al.</i> , 2018]	90.01	79.57	67.47
FPN [Lin <i>et al.</i> , 2017b]	90.65	80.06	68.26
Prithvi [Jakubik <i>et al.</i> , 2023]	66.14	66.21	49.74
Domain Adaptation			
UDAforRS [Li <i>et al.</i> , 2022]	75.16	72.42	57.49
BUS [Choe <i>et al.</i> , 2024]	60.22	59.21	42.35
Baseline Continual Learning			
LwF [Li and Hoiem, 2018]	90.22	78.94	67.02
LwM [Dhar <i>et al.</i> , 2019]	90.60	79.36	67.43
Replay [Rolnick <i>et al.</i> , 2019]	88.81	76.50	63.61
Class Incremental Learning			
SPPA [Lin <i>et al.</i> , 2022]	54.68	48.32	31.85
CCDA [Shenaj <i>et al.</i> , 2022]	78.90	72.90	57.00
Domain Incremental Learning			
MDIL-SS [Garg <i>et al.</i> , 2022]	88.62	85.36	71.99
GSMF-RS-DIL [Huang <i>et al.</i> , 2024]	88.83	85.02	71.25
MineC2FNet (ours)	92.33	84.10	73.64

Table 1: Performance comparison of different models across various models and learning paradigms.

where the numerator accumulates the KL divergence values, and the denominator normalizes it via the total number of selected pixels (with ϵ for numerical stability). This hierarchical and attentive strategy ensures that the student selectively learns only from the teacher’s most reliable predictions.

4.5 Training

Experimentation Setting. We implemented our framework using a Feature Pyramid Network (FPN) with a DenseNet-121 backbone, initialized with ImageNet pre-trained weights and modified to process 6-channel inputs (RGB, NIR, SWIR) at a resolution of 256×256 . The model was trained using the AdamW optimizer [Loshchilov and Hutter, 2019] with an initial learning rate of 1×10^{-3} , weight decay of 1×10^{-4} , and a batch size of 8 for a maximum of 100 epochs. Standard geometric augmentations, including random flips, rotations, and scaling, were applied to enhance generalization. All experiments were conducted on an NVIDIA RTX A4000 GPU.

Evaluation Metrics and Baselines. To assess performance, we benchmark MineC2FNet against five distinct learning paradigms: Transfer Learning (including the foundation model, e.g., Prithvi), Domain Adaptation, Baseline Continual Learning, Class Incremental Learning (CIL), and Domain Incremental Learning (DIL). Performance is evaluated using three standard metrics: *Pixel Accuracy*, *Mean F1 Score (mF1)*, and *Mean Intersection over Union (mIoU)*. More details can be found in the supplementary material.

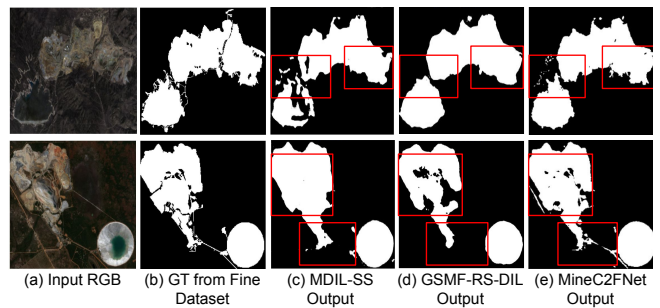


Figure 4: Segmentation results of MineC2FNet and several baseline models on the fine-grained test set.

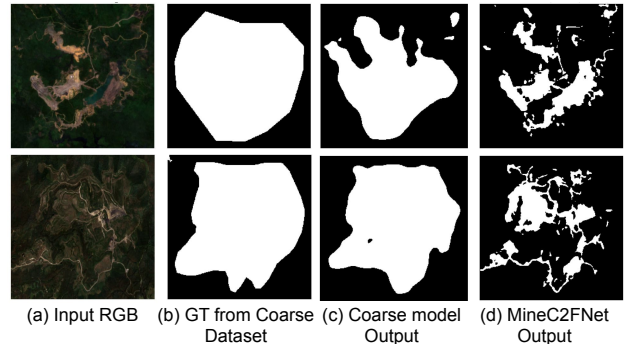


Figure 5: Through our framework, MineC2FNet produces more fine-grained output in the coarse dataset.

5 Results and Discussion

5.1 Overall Performance

Quantitative Analysis. Table 1 summarizes the performance of MineC2FNet against state-of-the-art methods. Our model, termed MineC2FNet, demonstrates superior performance, achieving the highest Accuracy (92.33%) and mIoU (73.64%) compared to different methods across five distinct learning categories. It is worth noting that while leading DIL methods like MDIL-SS achieve a slightly higher mF1 score (85.36% vs. 84.10%), our framework secures a clear advantage in mIoU, surpassing them by over 1.6 percentage points. This numerical superiority translates directly to visual precision, as shown in Figure 6, in which MineC2FNet successfully captures more detailed boundaries compared to the existing DIL models. Conversely, specialized CIL and Domain Adaptation methods struggle with this specific coarse-to-fine domain shift. Notably, methods such as SPPA (31.85%) and BUS (42.35%) perform significantly worse than even standard baseline continual learning approaches like LwF or LwM. This confirms that standard class-focused or domain adaptation strategies are ill-suited for this problem, whereas our approach successfully produces fine details while preserving coarse general knowledge.

We further compare our method with the coarse baseline on the coarse-grained dataset, as reported in Table 2. Although MineC2FNet achieves a lower mIoU (44.29%) than the coarse baseline (72.49%), this outcome is expected due to the imprecise annotations in the coarse dataset. The coarse

Metric	Coarse Baseline	MineC2FNet (Ours)
Accuracy	0.8733	0.7681
mF1	0.8331	0.5612
mIoU	0.7249	0.4429

Table 2: Performance comparison between the coarse baseline and the proposed MineC2FNet.

GF	CBAM	DR	Acc.	mF1	mIoU	Δ mIoU
✗	✗	✗	89.00	75.39	62.35	–
✓	✗	✗	90.31	76.72	64.35	+2.00
✓	✓	✗	91.33	79.15	67.79	+5.44
✓	✓	✓	91.08	79.84	68.41	+6.06

Table 3: Ablation study of Attentive Feature Injection.

baseline is trained and evaluated entirely on the source domain, and its predictions therefore closely match the coarse labels, which are known to contain inaccurate boundaries. In contrast, our model adapts to the target domain with finer and more precise annotations (see Figure 5), resulting in lower agreement when evaluated against coarse labels. This discrepancy does not indicate a failure of our approach; rather, it reflects superior boundary delineation while maintaining generalization by retaining useful knowledge from both coarse and fine domain. Evaluations across five Köppen–Geiger climate zones (Beck et al. 2018) confirmed the model’s global robustness and generalizability (see supplementary material).

Qualitative Analysis. Figure 6 highlights the precise segmentation masks generated by MineC2FNet, demonstrating its ability to accurately delineate complex boundaries. As shown in the second row, our model reduces false positives caused by noisy features more effectively than the baselines. Furthermore, when tested on the coarse dataset, our domain-adapted MineC2FNet yields fine-grained segmentation that reflects true features on the ground (Figure 5(d)). In contrast, training the model only on the coarse dataset inherits imprecise identification and poor boundary delineation (Figure 5(c)), underscoring the importance of our coarse-to-fine domain incremental learning.

Model Complexity and Efficiency. Finally, we evaluate MineC2FNet efficiency against the FPN baseline. The model achieves a substantial 5.4 point mIoU improvement, with a negligible speed reduction (13.38 to 11.00 FPS) due to added attention mechanisms. We consider this trade-off justified by the performance gain (detailed results in supplementary material).

5.2 Ablation Study

Impact of Attentive Feature Injection. We conducted ablation studies to clearly isolate the effects of each module within our attentive feature injection mechanism, i.e., Gated Fusion (GF), CBAM, and Diffusion Refinement (DR). Note that only RGB and NIR bands were used for this experiment. As shown in Table 3, while adding GF alone can improve performance, incorporating CBAM and DR yields a significant performance gain. The highest mIoU (68.41%) is

Strategy	Acc.	mF1	mIoU	Δ mIoU
No Distill. (Base)	89.00	75.39	62.35	–
Standard Distill.	89.38	75.79	62.59	+0.24
Image-level Sel.	90.42	78.79	67.17	+4.82
Pixel-level Sel.	91.14	79.30	67.84	+5.49
Hybrid Sel.	91.10	79.61	67.91	+5.56

Table 4: Comparison of different Attentive Knowledge Transfer strategies (all configurations include feature injection).

Band Comb.	Acc.	mF1	mIoU	Δ mIoU
RGB (Baseline)	87.08	71.12	57.09	–
RGB+NIR	89.00	75.39	62.35	+5.26
RGB+NIR+SWIR	89.68	79.29	67.29	+10.20

Table 5: Impact of different band combinations.

achieved when all three components are combined. This confirms that these modules contribute critically to the complete pipeline for optimal fusion of coarse and fine features.

Impact of Attentive Knowledge Transfer. Table 4 highlights the impact of different distillation methods. A model trained with standard distillation shows only marginal improvement over the baseline, confirming the risk of negative knowledge transfer. In contrast, our attentive distillation, at either image or pixel level, shows a large improvement (≥ 4.82 Δ mIoU). The hybrid method, distilling knowledge only from the teacher’s most accurate regions, achieves the highest performance, validating that a selective, hierarchical mechanism is critical for successful coarse-to-fine domain knowledge transfer.

Bands Comparison. As shown in Table 5, incorporating non-visible spectral bands is critical. While adding NIR significantly increases performance, the optimal results are achieved using the full RGB-NIR-SWIR combination. This underscores the value of NIR and SWIR bands in identifying distinct mining footprint features [Saputra *et al.*, 2025].

6 Conclusion

In this paper, we addressed the critical challenge of domain shift between coarse (abundant) and fine (scarce) datasets in training domain incremental learning model for mining footprint segmentation. We introduce MineC2FNet, a novel coarse-to-fine domain incremental framework. Our core contribution, an attentive distillation mechanism, proved highly effective, achieving a state-of-the-art mIoU of 73.64% by successfully selectively transferring knowledge from coarse to fine-grained data and outperforming other continual learning models. This work also introduced a new, expertly validated global dataset to facilitate further research in this domain. However, given our current limitation to binary segmentation, future work will extend this framework to complex multi-class segmentation of diverse mining and non-mining categories.

Acknowledgments

This study was supported in part by the Google Research Scholar Program, Australian Research Council LP200301160, and the Ford Foundation. The work of A. T. H. was partially supported by the Monash University Indonesia PhD Tuition Scholarship. We also sincerely thank John R. Owen for his contribution to the development of the training data.

References

- [Alfarra *et al.*, 2024] Motasem Alfarra, Zhipeng Cai, Adel Bibi, Bernard Ghanem, and Matthias Müller. Simcs: Simulation for domain incremental online continual segmentation. *Proceedings of the AAAI Conference on Artificial Intelligence*, 38(10):10795–10803, Mar. 2024.
- [Ang *et al.*, 2023] Michelle Li Ern Ang, John R. Owen, Christopher N. Gibbins, Éléonore Lèbre, Deanna Kemp, Muhamad Risqi U. Saputra, Jo-Anne Everingham, and Alex M. Lechner. Systematic review of gis and remote sensing applications for assessing the socioeconomic impacts of mining. *The Journal of Environment & Development*, 32(3):243–273, 2023.
- [Beck *et al.*, 2018] Hylke E. Beck, Niklaus E. Zimmermann, Tim R. McVicar, Noemi Vergopolan, Alexis Berg, and Eric F. Wood. Present and future köppen-geiger climate classification maps at 1-km resolution. *Scientific Data*, 5(1):180214, Oct 2018.
- [Cai *et al.*, 2023] Zhiwen Cai, Haodong Wei, Qiong Hu, Wei Zhou, Xinyu Zhang, Wenjie Jin, Ling Wang, Shuxia Yu, Zhen Wang, Baodong Xu, et al. Learning spectral-spatial representations from vhr images for fine-scale crop type mapping: A case study of rice-crayfish field extraction in south china. *ISPRS Journal of Photogrammetry and Remote Sensing*, 199:28–39, 2023.
- [Chen *et al.*, 2018] Liang-Chieh Chen, Yukun Zhu, George Papandreou, Florian Schroff, and Hartwig Adam. Encoder-decoder with atrous separable convolution for semantic image segmentation, 2018.
- [Chen *et al.*, 2024] Hao Chen, Wen Yang, Li Liu, and Gui-Song Xia. Coarse-to-fine semantic segmentation of satellite images. *ISPRS Journal of Photogrammetry and Remote Sensing*, 217:1–17, 2024.
- [Choe *et al.*, 2024] Seun-An Choe, Ah-Hyung Shin, Keon-Hee Park, Jinwoo Choi, and Gyeong-Moon Park. Open-set domain adaptation for semantic segmentation. In *Proceedings of the IEEE/CVF Conference on Computer Vision and Pattern Recognition*, pages 23943–23953, 2024.
- [Das *et al.*, 2023] Anurag Das, Yongqin Xian, Yang He, Zeynep Akata, and Bernt Schiele. Urban scene semantic segmentation with low-cost coarse annotation. In *2023 IEEE/CVF Winter Conference on Applications of Computer Vision (WACV)*, pages 5967–5976, 2023.
- [Dhar *et al.*, 2019] Prithviraj Dhar, Rajat Vikram Singh, Kuan-Chuan Peng, Ziyang Wu, and Rama Chellappa. Learning without memorizing. In *Proceedings of the IEEE/CVF conference on computer vision and pattern recognition*, pages 5138–5146, 2019.
- [Garg *et al.*, 2022] Prachi Garg, Rohit Saluja, Vineeth N Balasubramanian, Chetan Arora, Anbumani Subramanian, and CV Jawahar. Multi-domain incremental learning for semantic segmentation. In *Proceedings of the IEEE/CVF Winter Conference on Applications of Computer Vision*, pages 761–771, 2022.
- [Huang *et al.*, 2024] Wubiao Huang, Mingtao Ding, and Fei Deng. Domain-incremental learning for remote sensing semantic segmentation with multifeature constraints in graph space. *IEEE Transactions on Geoscience and Remote Sensing*, 62:1–15, 2024.
- [Jakubik *et al.*, 2023] Johannes Jakubik, Sujit Roy, C. E. Phillips, Paolo Fraccaro, Denys Godwin, Bianca Zadrozny, Daniela Szwarcman, Carlos Gomes, Gabby Nyirjesy, Blair Edwards, Daiki Kimura, Naomi Simumba, Linsong Chu, S. Karthik Mukkavilli, Devyani Lambhate, Kamal Das, Ranjini Bangalore, Dario Oliveira, Michal Muszynski, Kumar Ankur, Muthukumaran Ramasubramanian, Iksha Gurung, Sam Khallaghi, Hanxi, Li, Michael Cecil, Maryam Ahmadi, Fatemeh Kordi, Hamed Alemohammad, Manil Maskey, Raghu Ganti, Kommy Weldemariam, and Rahul Ramachandran. Foundation models for generalist geospatial artificial intelligence, 2023.
- [Kemp and Owen, 2025] Deanna Kemp and John R. Owen. Global mining and the production of inequality: a case for continued inquiry. *World Development Perspectives*, 39:100708, 2025.
- [Lechner *et al.*, 2016] Alex Mark Lechner, Owen Kassulke, and Corinne Unger. Spatial assessment of open cut coal mining progressive rehabilitation to support the monitoring of rehabilitation liabilities. *Resources Policy*, 50:234–243, December 2016. Publisher Copyright: © 2016 Elsevier Ltd Copyright: Copyright 2017 Elsevier B.V., All rights reserved.
- [Lechner *et al.*, 2017] Alex M. Lechner, Neil McIntyre, Katherine Witt, Christopher M. Raymond, Sven Arnold, Margaretha Scott, and Will Rifkin. Challenges of integrated modelling in mining regions to address social, environmental and economic impacts. *Environmental Modelling & Software*, 93:268–281, 2017.
- [Lechner *et al.*, 2019] Alex M Lechner, John Owen, Michelle Li Ern Ang, Mansour Edraki, Nor Aklima Che Awang, and Deanna Kemp. Historical socio-environmental assessment of resource development footprints using remote sensing. *Remote Sensing Applications: Society and Environment*, 15:100236, 2019.
- [Li and Hoiem, 2018] Zhizhong Li and Derek Hoiem. Learning without forgetting. *IEEE Transactions on Pattern Analysis and Machine Intelligence*, 40(12):2935–2947, 2018.
- [Li *et al.*, 2022] Weitao Li, Hui Gao, Yi Su, and Bifon Manyura Momanyi. Unsupervised domain adapta-

- tion for remote sensing semantic segmentation with transformer. *Remote Sensing*, 14(19), 2022.
- [Lin *et al.*, 2017a] Guosheng Lin, Anton Milan, Chunhua Shen, and Ian Reid. Refinenet: Multi-path refinement networks for high-resolution semantic segmentation. In *2017 IEEE Conference on Computer Vision and Pattern Recognition (CVPR)*, pages 5168–5177, 2017.
- [Lin *et al.*, 2017b] Tsung-Yi Lin, Piotr Dollár, Ross Girshick, Kaiming He, Bharath Hariharan, and Serge Belongie. Feature pyramid networks for object detection. In *2017 IEEE Conference on Computer Vision and Pattern Recognition (CVPR)*, pages 936–944, 2017.
- [Lin *et al.*, 2022] Zihan Lin, Zilei Wang, and Yixin Zhang. Continual semantic segmentation via structure preserving and projected feature alignment. In Shai Avidan, Gabriel Brostow, Moustapha Cissé, Giovanni Maria Farinella, and Tal Hassner, editors, *Computer Vision – ECCV 2022*, pages 345–361, Cham, 2022. Springer Nature Switzerland.
- [Loshchilov and Hutter, 2019] Ilya Loshchilov and Frank Hutter. Decoupled weight decay regularization, 2019.
- [Mao *et al.*, 2023] Anqi Mao, Mehryar Mohri, and Yutao Zhong. Cross-entropy loss functions: Theoretical analysis and applications, 2023.
- [Maus *et al.*, 2020] Victor Maus, Stefan Giljum, Jakob Gutschlhofer, Dieison M. da Silva, Michael Probst, Sidnei L. B. Gass, Sebastian Luckeneder, Mirko Lieber, and Ian McCallum. A global-scale data set of mining areas. *Scientific Data*, 7(1):289, Sep 2020.
- [Maus *et al.*, 2022] Victor Maus, Dieison M da Silva, Jakob Gutschlhofer, Robson da Rosa, Stefan Giljum, Sidnei L B Gass, Sebastian Luckeneder, Mirko Lieber, and Ian McCallum. Global-scale mining polygons (Version 2), 2022.
- [Owen *et al.*, 2023] John R. Owen, Deanna Kemp, Alex M. Lechner, Jill Harris, Ruilian Zhang, and Éléonore Lèbre. Energy transition minerals and their intersection with land-connected peoples. *Nature Sustainability*, 6(2):203–211, Feb 2023.
- [Qiao *et al.*, 2024] Qinghua Qiao, Yanyue Li, and Huaquan Lv. Open-pit mining area extraction using multispectral remote sensing images: A deep learning extraction method based on transformer. *Applied Sciences*, 14(14), 2024.
- [Rolnick *et al.*, 2019] David Rolnick, Arun Ahuja, Jonathan Schwarz, Timothy P. Lillicrap, and Greg Wayne. Experience replay for continual learning, 2019.
- [Ronneberger *et al.*, 2015] Olaf Ronneberger, Philipp Fischer, and Thomas Brox. U-net: Convolutional networks for biomedical image segmentation. *ArXiv*, abs/1505.04597, 2015.
- [Saputra *et al.*, 2025] Muhamad Risqi U Saputra, Irfan Dwiki Bhaswara, Bahrul Ilmi Nasution, Michelle Ang Li Ern, Nur Laily Romadhotul Husna, Tahjudil Witra, Vicky Feliren, John R Owen, Deanna Kemp, and Alex M Lechner. Multi-modal deep learning approaches to semantic segmentation of mining footprints with multi-spectral satellite imagery. *Remote Sensing of Environment*, 318:114584, 2025.
- [Shenaj *et al.*, 2022] Donald Shenaj, Francesco Barbato, Umberto Michieli, and Pietro Zanuttigh. Continual coarse-to-fine domain adaptation in semantic segmentation. *Image and Vision Computing*, 121:104426, 2022.
- [Sonter *et al.*, 2018] Laura J Sonter, Saleem H Ali, and James E M Watson. Mining and biodiversity: key issues and research needs in conservation science. *Proc Biol Sci*, 285(1892), December 2018.
- [Sudre *et al.*, 2017] Carole H. Sudre, Wenqi Li, Tom Vercauteren, Sebastien Ourselin, and M. Jorge Cardoso. *Generalised Dice Overlap as a Deep Learning Loss Function for Highly Unbalanced Segmentations*, page 240–248. Springer International Publishing, 2017.
- [Takikawa *et al.*, 2019] Towaki Takikawa, David Acuna, Varun Jampani, and Sanja Fidler. Gated-scnn: Gated shape cnns for semantic segmentation, 2019.
- [Tong *et al.*, 2020] Xin-Yi Tong, Gui-Song Xia, Qikai Lu, Huanfeng Shen, Shengyang Li, Shucheng You, and Liangpei Zhang. Land-cover classification with high-resolution remote sensing images using transferable deep models. *Remote Sensing of Environment*, 237:111322, 2020.
- [Werner *et al.*, 2020] Tim T Werner, Gavin M Mudd, Aafke M Schipper, Mark AJ Huijbregts, Lakshay Taneja, and Stephen A Northey. Global-scale remote sensing of mine areas and analysis of factors explaining their extent. *Global Environmental Change*, 60:102007, 2020.
- [Wieland *et al.*, 2023] Marc Wieland, Sandro Martinis, Ralph Kiefl, and Veronika Gstaiger. Semantic segmentation of water bodies in very high-resolution satellite and aerial images. *Remote Sensing of Environment*, 287:113452, 2023.
- [Woo *et al.*, 2018] Sanghyun Woo, Jongchan Park, Joon-Young Lee, and In So Kweon. Cbam: Convolutional block attention module. In *Computer Vision – ECCV 2018: 15th European Conference, Munich, Germany, September 8–14, 2018, Proceedings, Part VII*, page 3–19, Berlin, Heidelberg, 2018. Springer-Verlag.
- [Zhao *et al.*, 2019] Shuai Zhao, Boxi Wu, Wenqing Chu, Yao Hu, and Deng Cai. Correlation maximized structural similarity loss for semantic segmentation, 2019.
- [Zhu *et al.*, 2025] Xiaoqian Zhu, Xiangrong Zhang, Tianyang Zhang, Chaowei Fang, Xu Tang, and Licheng Jiao. Regionmatch: Pixel-region collaboration for semi-supervised semantic segmentation in remote sensing images. In James Kwok, editor, *Proceedings of the Thirty-Fourth International Joint Conference on Artificial Intelligence, IJCAI-25*, pages 2530–2538. International Joint Conferences on Artificial Intelligence Organization, 8 2025. Main Track.

7 Supplementary Material

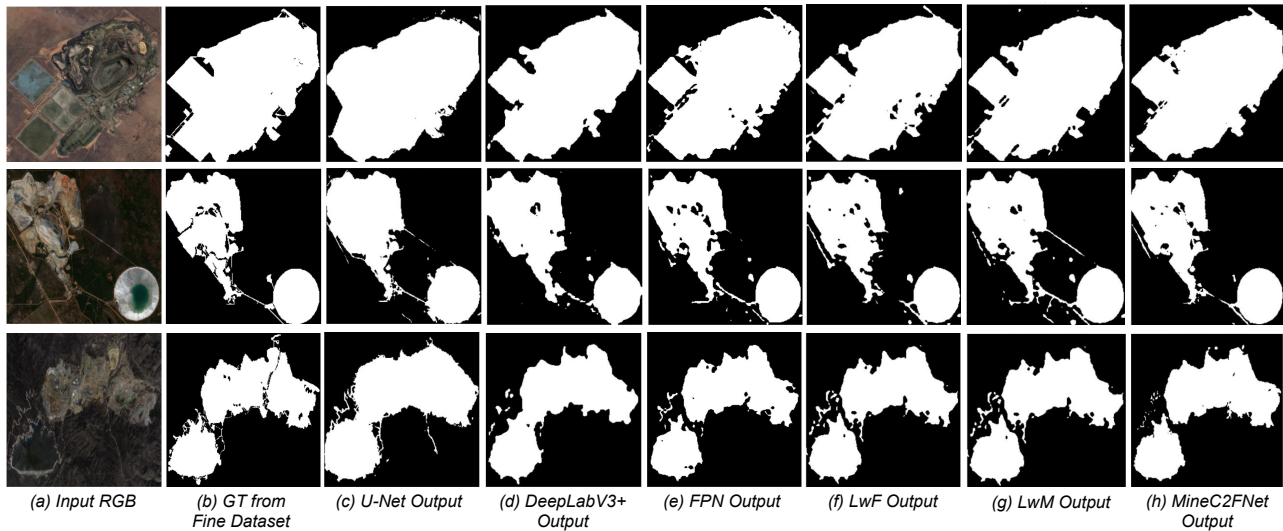


Figure 6: Segmentation results of MineC2FNet and several baseline models on the fine-grained test set.

Mine ID	Mine Name	Country	Commodity	Climate	Region	Sensor
3	Alpamarca	Peru	PbZnCu	5	South America	Sentinel 2
5	Atacocha	Peru	PbZnCu	5	South America	Sentinel 2
14	Carmen_de_Andacollo	Chile	Cu	2	South America	Sentinel 2
17	Cerro_de_Pasco	Peru	PbZnCu	5	South America	Sentinel 2
18	Cerro_Lindo	Peru	PbZnCu	2	South America	Sentinel 2
29	Flying_Fox_Spotted_Quoll	Australia	Ni S	2	Oceania	Sentinel 2
31	Impala_Group	South Africa	PGEs	2	Africa	Sentinel 2
32	Julcani	Peru	PbZnCu	5	South America	Sentinel 2
34	Kimberley	South Africa	Diamonds	2	Africa	Sentinel 2
37	Letseng	Lesotho	Diamonds	5	Africa	Sentinel 2
38	Magellan	Australia	PbZn	2	Oceania	Sentinel 2
39	Mantoverde	Chile	Cu	2	South America	Sentinel 2
41	McArthur_River_Australia	Australia	PbZn	2	Oceania	Sentinel 2
43	Mogalakwena	South Africa	PGEs	2	Africa	Sentinel 2
44	Mototolo	South Africa	PGEs	3	Africa	Sentinel 2
46	Nkomati	South Africa	Ni S	3	Africa	Sentinel 2
47	North_Mara	Tanzania	Au	1	Africa	Sentinel 2
50	Paracatu	Brazil	Au	1	South America	Sentinel 2
51	Pinto_Valley	USA	CuMo	2	North America	Sentinel 2
55	Punitaqui	Chile	CuAg	2	South America	Sentinel 2
58	Stawell	Australia	Au	3	Oceania	Sentinel 2
60	Tara	Ireland	PbZn	3	Europe	Sentinel 2
62	Tizapa	Mexico	PbZnCu	1	North America	Sentinel 2
64	Two_Rivers	South Africa	PGEs	3	Africa	Sentinel 2
65	Union_North_South	South Africa	PGEs	2	Africa	Sentinel 2
66	Velardena	Mexico	PbZnCu	2	North America	Sentinel 2
68	Waihi	New Zealand	AuAg	3	Oceania	Sentinel 2
69	Yauli	Peru	PbZnCu	5	South America	Sentinel 2
70	Yauricocha	Peru	PbZnCu	5	South America	Sentinel 2
72	Zawar	India	PbZn	2	Asia	Sentinel 2
74	Agbaou	Côte d'Ivoire	Au	1	Africa	Landsat 8
76	Batu_Hijau	Indonesia	CuAu	1	Asia	Landsat 8

Table 6: Details of the Training Set (153 images) (Continued on next page).

Mine ID	Mine Name	Country	Commodity	Climate	Region	Sensor
78	Bokoni	South Africa	PGEs	2	Africa	Landsat 8
79	Bolivar	Mexico	CuAu	3	North America	Landsat 8
80	Bonikro	Côte d'Ivoire	AuAg	1	Africa	Landsat 8
81	Boss_Mining_Group	Dem. Rep. Congo	CuCo	3	Africa	Landsat 8
82	Cadia_Group	Australia	AuCu	3	Oceania	Landsat 8
85	Cerro_Corona	Peru	AuCu	5	South America	Landsat 8
88	Collahuasi	Chile	CuMo	2	South America	Landsat 8
89	Costerfield	Australia	Au	2	Oceania	Landsat 8
90	Cozamin	Mexico	PbZnCu	2	North America	Landsat 8
91	Cracow	Australia	AuAg	3	Oceania	Landsat 8
92	Cuajone	Peru	CuMo	2	South America	Landsat 8
94	De_Grussa	Australia	CuAu	2	Oceania	Landsat 8
98	Essakane	Burkina Faso	Au	2	Africa	Landsat 8
100	Fosterville	Australia	Au	2	Oceania	Landsat 8
101	Franke	Chile	Cu	2	South America	Landsat 8
103	Guelb_Moghrein	Mauritania	CuAu	2	Africa	Landsat 8
104	Hidden_Valley	Papua New Guinea	AuAg	3	Oceania	Landsat 8
105	Highland_Valley	Canada	CuMo	4	North America	Landsat 8
106	Huckleberry	Canada	CuAu	4	North America	Landsat 8
108	Kanmantoo	Australia	CuAu	2	Oceania	Landsat 8
109	Kansanshi	Zambia	CuAu	3	Africa	Landsat 8
110	Khetri_Group	India	Cu	2	Asia	Landsat 8
111	Kittila	Finland	AuAg	4	Europe	Landsat 8
114	Lady_Annie	Australia	Cu	2	Oceania	Landsat 8
115	Lagunas_Norte	Peru	Au	5	South America	Landsat 8
116	Lisheen	Ireland	PbZn	3	Europe	Landsat 8
118	Macraes	New Zealand	Au	3	Oceania	Landsat 8
119	Marlin	Guatemala	AuAg	3	North America	Landsat 8
121	Mission	USA	Cu	2	North America	Landsat 8
122	Mount_Carlton	Australia	AuCu	1	Oceania	Landsat 8
123	Mount_Garnet_Surveyor	Australia	PbZnCu	3	Oceania	Landsat 8
124	Mount_Milligan	Canada	CuAu	4	North America	Landsat 8
126	Myra_Falls	Canada	PbZnCu	3	North America	Landsat 8
127	Olimpiada	Russia	AuAg	4	Europe	Landsat 8
129	Oyu_Tolgoi	Mongolia	CuAu	2	Asia	Landsat 8
130	Parkers_Mineral_Hill	Australia	PbZnCu	2	Oceania	Landsat 8
131	Peak	Australia	AuCu	2	Oceania	Landsat 8
132	Pierina	Peru	Au	5	South America	Landsat 8
133	Pilanesberg	South Africa	PGEs	2	Africa	Landsat 8
134	Quebrada_Blanca	Chile	Cu	2	South America	Landsat 8
136	Ranger	Australia	U	1	Oceania	Landsat 8
137	Ray	USA	Cu	2	North America	Landsat 8
138	Rum_Jungle	Australia	U-Cu	1	Oceania	Landsat 8
139	Salobo	Brazil	CuAu	1	South America	Landsat 8
140	Savannah_Sally_Malay	Australia	Ni S	2	Oceania	Landsat 8
141	Sierra_Gorda	Chile	CuMo	2	South America	Landsat 8
142	Skorpion	Namibia	PbZn	2	Africa	Landsat 8
143	Sossego	Brazil	CuAu	1	South America	Landsat 8
145	Tenke_Fungurume	Dem. Rep. Congo	CuCo	3	Africa	Landsat 8
147	Togaruci_Gosowong	Indonesia	AuAg	1	Asia	Landsat 8
148	Toledo_Carmen_Lutopan	Philippines	CuAu	1	Asia	Landsat 8
149	Toquepala	Peru	CuMo	2	South America	Landsat 8
150	Tres_Valles	Chile	Cu	2	South America	Landsat 8
151	Trident_Sentinel	Zambia	Cu	1	Africa	Landsat 8
152	Venetia	South Africa	Diamonds	2	Africa	Landsat 8

Table 6: Details of the Training Set (153 images) (Continued on next page).

Mine ID	Mine Name	Country	Commodity	Climate	Region	Sensor
153	Wetar	Indonesia	Cu	1	Asia	Landsat 8
154	Akyem	Ghana	Au	1	Africa	Landsat 8
156	Broken_Hill	Australia	PbZn	2	Oceania	Landsat 8
157	Century	Australia	PbZn	2	Oceania	Landsat 8
158	Challenger	Australia	Au	2	Oceania	Landsat 8
160	Cobar_CSA	Australia	CuAg	2	Oceania	Landsat 8
161	Ernest_Henry	Australia	CuAu	2	Oceania	Landsat 8
164	Henderson	USA	Mo	4	North America	Landsat 8
165	Kalgoorlie_SuperPit	Australia	Au	2	Oceania	Landsat 8
166	Kevitsa	Finland	Ni S	4	Europe	Landsat 8
169	La_Caridad	Mexico	CuMo	2	North America	Landsat 8
171	Lac_des_Iles	Canada	PGEs	4	North America	Landsat 8
172	Langlois	Canada	PbZnCu	4	North America	Landsat 8
173	Las_Cruces	Spain	Cu	3	Europe	Landsat 8
175	Madero	Mexico	PbZnCu	2	North America	Landsat 8
176	Malanjhand	India	Cu	1	Asia	Landsat 8
177	Mary_Kathleen	Australia	U	2	Oceania	Landsat 8
178	Masbate	Indonesia	AuAg	1	Asia	Landsat 8
179	Miaogou_Sanguikou	China	PbZnCu	2	Asia	Landsat 8
180	Mount_Lyell	Australia	CuAu	3	Oceania	Landsat 8
182	Nifty	Australia	Cu	2	Oceania	Landsat 8
183	Northparkes	Australia	CuAu	2	Oceania	Landsat 8
184	Olympic_Dam	Australia	CuAu	2	Oceania	Landsat 8
185	Orlovsky	Kazakhstan	PbZnCu	4	Asia	Landsat 8
186	Prominent_Hill	Australia	CuAu	2	Oceania	Landsat 8
187	Pyhasalmi	Finland	PbZnCu	4	Europe	Landsat 8
189	Reefton	New Zealand	Au	3	Oceania	Landsat 8
191	Rosebery	Australia	PbZnCu	3	Oceania	Landsat 8
193	Tarkwa	Ghana	Au	1	Africa	Landsat 8
194	Telfer	Australia	AuCu	2	Oceania	Landsat 8
195	Tritton	Australia	Cu	2	Oceania	Landsat 8
196	Twangiza	Congo-DRC	Au	3	Africa	Landsat 8
198	Zinkgruvan	Sweden	PbZnCu	4	Europe	Landsat 8
199	Bald_Mountain	USA	Au	4	North America	Landsat 8
201	Chapada	Brazil	CuAu	1	South America	Landsat 8
204	El_Salvador	Chile	CuMo	2	South America	Landsat 8
205	Galena	USA	PbZnCu	4	North America	Landsat 8
206	Ghaghoo	Botswana	Diamonds	2	Africa	Landsat 8
207	Golden_Sunlight	USA	Au	2	North America	Landsat 8
210	Ity	Côte d'Ivoire	Au	1	Africa	Landsat 8
211	Letlhakane	Botswana	Diamonds	2	Africa	Landsat 8
212	Lihir	Papua New Guinea	AuAg	1	Oceania	Landsat 8
214	Marigold_JV	USA	Au	2	North America	Landsat 8
215	Mount_Polley	Canada	CuAu	4	North America	Landsat 8
217	Onca_Puma	Brazil	Ni Lat	1	South America	Landsat 8
218	Pajingo	Australia	AuAg	2	Oceania	Landsat 8
219	Phoenix	USA	AuCu	2	North America	Landsat 8
220	Phu_Kham	Laos	CuAu	1	Asia	Landsat 8
222	Sabodala	Senegal	Au	1	Africa	Landsat 8
224	Thompson	Canada	Ni S	4	North America	Landsat 8
225	Unki	Zimbabwe	PGEs	3	Africa	Landsat 8
226	Veladero	Argentina	Au	5	South America	Landsat 8

Table 6: Details of the Training Set (153 images).

Mine ID	Mine Name	Country	Commodity	Climate	Region	Sensor
1	Afton_New_Afton	Canada	CuAu	2	North America	Sentinel
2	Ahafo	Ghana	Au	1	Africa	Sentinel
7	Black_Mountain	Mexico	PbZnCu	1	North America	Sentinel
11	Campo_Morado	Peru	PbZnCu	1	South America	Sentinel
12	Candelaria	Chile	Cu	2	South America	Sentinel
13	Cannington	Australia	PbZn	2	Oceania	Sentinel
16	Cerro_Corona	Peru	PbZnCu	5	South America	Sentinel
20	Chatree	Thailand	Au	1	Asia	Sentinel
21	Climax	USA	Mo	4	North America	Sentinel
22	Constancia	Peru	CuAu	5	South America	Sentinel
23	Contonga	Peru	PbZnCu	5	South America	Sentinel
25	El_Porvenir	Peru	PbZnCu	5	South America	Sentinel
26	El_Soldado	Chile	Cu	5	South America	Sentinel
27	El_Teniente	Chile	CuMo	5	South America	Sentinel
28	Erdenet	Mongolia	CuMo	4	Asia	Sentinel
35	Kinsevere	DRC	Cu	3	Africa	Landsat
42	Modikwa	South Africa	PGEs	3	Africa	Sentinel
48	Padcal	Philippines	CuAu	1	Asia	Landsat
52	Polska_Miedz	Poland	CuAg	4	Europe	Landsat
53	Priargunsky	Russia	U	4	Europe	Landsat
56	Sepon	Laos	CuAu	1	Asia	Landsat
61	Thompson	Canada	NiS	4	North America	Landsat

Table 7: Details of the Validation Set (22 images).

Mine Name	Country	Commodity	Climate	Region	Sensor
Bulyanhulu	Tanzania	Au	1	Africa	Sentinel 2
Cosala_Nuestra	Mexico	PbZnCu	1	North America	Sentinel 2
Chirano	Ghana	Au	1	Africa	Landsat 8
Antucoya	Chile	Au	3	South America	Sentinel 2
Goro	New Caledonia	Ni Lat	1	Oceania	Landsat 8
Pueblo_Viejo	Dom. Rep.	Au	1	North America	Sentinel 2
Tongon	Côte d’Ivoire	Au	1	Africa	Sentinel 2
Santa_Rita	Brazil	Ni S	2	South America	Landsat 8
Orapa	Botswana	Cu	2	Africa	Sentinel 2
Tati	Botswana	Ni S	2	Africa	Landsat 8
Marula	South Africa	PGEs	3	Africa	Sentinel 2
Mount_Isa	Australia	PbZnCu	2	Oceania	Landsat 8
Gabriela_Mistral	Chile	CuMo	2	South America	Landsat 8
Centinela	Chile	Cu	1	South America	Sentinel 2
Milpillas	Mexico	Cu	1	North America	Landsat 8
Damtshee	Botswana	Diamonds	2	Africa	Landsat 8
Spence	Chile	Cu	2	South America	Landsat 8
Antucoya	Chile	Cu	2	South America	Sentinel 2
Ravensthorpe	Australia	Ni Lat	1	Oceania	Landsat 8
Mantos_Blancos	Chile	Cu	2	South America	Landsat 8
Orapa	Botswana	Diamonds	2	Africa	Landsat 8
Granny_Smith	Australia	Au	2	Oceania	Landsat 8
Goldstrike	USA	Au	2	North America	Landsat 8
Cerro_Verde	Peru	Cu	2	South America	Sentinel 2
Endeavour	Australia	PbZn	2	Oceania	Landsat 8
Cerro_Color	Chile	Cu	2	South America	Landsat 8
Silver_Bell	USA	Cu	3	North America	Sentinel 2
Robinson	USA	CuMo	2	North America	Landsat 8
Jwaneng	Botswana	Diamonds	1	Africa	Landsat 8
Argyle	Australia	Diamonds	1	Oceania	Landsat 8
Konkola_Nchanga	Zambia	Cu	1	Africa	Landsat 8
Bafokeng_Rasimone	South Africa	PGEs	2	Africa	Sentinel 2
Ejimshan	China	Cu	3	Asia	Landsat 8
Shishen	China	Cu	3	Asia	Landsat 8
Kamoa	DRC	Ni S	1	Africa	Landsat 8
Voorspoed	South Africa	Diamonds	3	Africa	Landsat 8
Mount_Rawdon	Australia	AuAg	3	Oceania	Landsat 8
Boddington	Australia	AuCu	3	Oceania	Landsat 8
Frontier	DRC	Au	3	Africa	Sentinel 2
Bingham_Canyon	USA	CuMoAu	4	North America	Landsat 8
Los_Pelambres	Chile	CuMo	5	South America	Landsat 8
Antamina	Peru	PbZnCu	5	South America	Sentinel 2
Porgera	Papua New Guinea	AuAg	3	Oceania	Landsat 8
Santa_Rita	Brazil	Ni S	1	South America	Landsat 8

Table 8: Details of the Test Set (44 images).

Dataset	Input Size	Phase	F1 Score	Mean IoU	Accuracy
FineDataset	128	Training	0.8854	0.7451	0.9501
		Validation	0.6878	0.5391	0.8823
		Testing	0.6808	0.5459	0.8692
FineDataset + Patching	128	Training	0.9435	0.7832	0.9764
		Validation	0.6732	0.6324	0.9244
		Testing	0.5373	0.4315	0.8447
FineDataset	256	Training	0.9333	0.8444	0.9715
		Validation	0.7574	0.6193	0.9034
		Testing	0.7539	0.6235	0.8900
FineDataset	512	Training	0.9290	0.8448	0.9709
		Validation	0.7547	0.6240	0.9121
		Testing	0.7596	0.6391	0.9025
CoarseDataset	128	Training	0.9475	0.8913	0.9576
		Validation	0.8411	0.7359	0.8779
		Testing	0.8358	0.7285	0.8778
CoarseDataset + Patching	128	Training	0.8399	0.6354	0.8662
		Validation	0.6628	0.5884	0.8153
		Testing	0.6366	0.5089	0.7241
CoarseDataset	256	Training	0.9071	0.8205	0.9250
		Validation	0.8477	0.7450	0.8804
		Testing	0.8438	0.7402	0.8811
CoarseDataset	512	Training	0.8710	0.7663	0.8972
		Validation	0.8380	0.7337	0.8760
		Testing	0.8336	0.7276	0.8756

Table 9: Performance comparison for different input sizes and the effect of patching on both Fine and Coarse datasets. Each model was evaluated on its corresponding dataset (FineDataset on the Fine test set and CoarseDataset on the Coarse test set).

Dataset	Total Images	Min Image Size	F1 Score	Mean IoU	Accuracy
Full Coarse	44,319	7×7	0.5599	0.4231	0.7060
Coarse-128	12,155	128×128	0.5841	0.4443	0.7298
Coarse-FineFiltered	1,380	374×566	0.5931	0.4552	0.7334
Coarse-FineFiltered-100	1,280	669×362	0.5727	0.4335	0.7167

Table 10: Performance on the fine dataset test split after pre-training on coarse datasets of varying sizes and compositions.

7.1 Fine Datasets Details

The fine dataset comprises a total of 219 images, which are split into training (153 images), validation (22 images), and test (44 images) sets. To ensure a robust evaluation across diverse global conditions, the dataset is sourced from 39 countries across 6 continents: North America, South America, Africa, Asia, Europe, and Oceania. The dataset is also balanced across five major climate zones, grouped according to the Köppen-Geiger classification system: (1) Tropical, (2) Arid, (3) Temperate, (4) Cold, and (5) Polar. This comprehensive distribution ensures the model is tested against a wide variety of geographical and environmental backdrops.

Training Set The training set consists of 153 images, covering a diverse range of mine types, climates, and geographic locations.

Validation Set The validation set contains 22 images, used for tuning model hyperparameters during training.

Test Set The test set comprises 44 images, held out to provide an unbiased evaluation of the final model’s performance.

7.2 Supplementary Experiments

To determine the optimal hyperparameters and dataset configurations for our pipeline, we conducted a series of ablation studies. These experiments analyze the impact of input image resolution, the use of patching, and the composition of the coarse dataset on model performance. Figure 1 visually corroborates our findings and highlights the limitations of other approaches. As shown, the outputs from standard segmentation architectures (c-e) and other continual learning strategies (f-g) struggle with the task’s complexity, producing incomplete masks that fail to capture fine, connecting structures. In contrast, the predictions from our proposed method, MiningNet (h) are qualitatively superior, aligning almost perfectly with the ground truth (b) by accurately delineating complex boundaries to generate a complete and precise segmentation mask.

Continual Learning Strategy To validate our framework’s core design, we compare it against established Continual Learning (CL) strategies. For our coarse-to-fine task, these methods are re-contextualized: the ”continual” process involves transferring knowledge from a teacher model (trained on coarse data) to a student model (trained on fine data). We adapted LwF [Li and Hoiem, 2018], which uses knowledge distillation (KD) as a regularizer to preserve the teacher’s general knowledge, and LwM [Dhar *et al.*, 2019], which in our case uses attention distillation to focus the student model on critical boundary regions. Finally, we adopt a selective Replay strategy [Rolnick *et al.*, 2019] inspired by experience replay in reinforcement learning. In our approach, we filter coarse-labeled samples based on a predefined quality heuristic: a model trained on fine data is used to generate predictions on the coarse images, and only samples with high consistency between the prediction and the coarse label are retained for joint training. While these CL adaptations offer benefits, our proposed MiningNet still surpasses them, demonstrating the advantage of its advanced attentive distillation mechanism for more effective and targeted knowledge transfer.

Impact of Input Resolution and Patching We first evaluated the effect of different input sizes (128×128 , 256×256 , and 512×512 pixels) on both the Fine and Coarse datasets. Additionally, we investigated whether an image patching strategy could improve performance. For this experiment, we utilized the patchify Python library, a tool designed to split images into a grid of smaller, potentially overlapping patches. We configured it to extract patches of 128×128 pixels with a step size of 128 to avoid overlap between adjacent patches. The hypothesis was that training on these patches would allow the model to learn more fine-grained local features from the original high-resolution imagery, which is otherwise lost when down-scaling the entire image. By processing these high-detail patches, we aimed to improve the model’s ability to segment intricate boundaries. The results for all experiments are detailed in Table 4.

From the results, it is evident that an input size of 256×256 or 512×512 provides the best performance for the fine-tuned model, with the 512×512 input achieving a slightly higher testing F1-score (0.7596 vs 0.7539). For the coarse dataset, the 256×256 input size clearly outperforms the others, achieving the highest testing F1-score of 0.8438. Notably, the application of patching to the 128×128 input proved to be detrimental, significantly degrading performance for both datasets. This suggests that the model benefits more from a complete view of the image, even at a lower resolution, than from localized patches. Given the trade-off between performance and computational cost, an input size of 256×256 was selected as the optimal choice for our main experiments.

Impact of Coarse Dataset Composition The coarse dataset serves as a large-scale pre-training corpus. Our initial set contained 44,319 images with extreme variations in dimension, from as small as 7×7 pixels to over 1300×1400 pixels. A significant portion of this dataset (32,164 images) consisted of very low-resolution images smaller than 128×128 pixels. To find the most effective pre-training data, we tested several filtering strategies based on minimum image dimensions. We evaluated the full, unfiltered dataset; a version filtered to include only images of at least 128×128 pixels (‘Coarse-128’); and a more targeted version (‘Coarse-FineFiltered’) designed to align the coarse data’s characteristics with our fine dataset, using the smallest fine mine’s area (9.81 km^2) as a benchmark. The performance of a model pre-trained on each of these coarse dataset versions was then evaluated on the fine dataset’s test split. The results are shown in Table 5.

The results demonstrate the critical importance of curating the coarse dataset. Using the full, unfiltered set of 44,319 images yields the poorest performance, likely due to the noise introduced by the thousands of very low-resolution images. Filtering the data to remove images smaller than 128×128 pixels (‘Coarse-128’) provides a notable improvement. However, the best results are achieved with the Coarse-FineFiltered set. This approach, which curated the coarse data to align with the area characteristics of the fine dataset, produced the highest F1-score of 0.5931. This indicates that pre-training on a well-curated, domain-relevant dataset is more effective than using a larger, noisier one.

7.3 Training

In this sub-section, we describe how to train the model, including data augmentation, model configuration, optimization parameters, evaluation metrics, and baselines.

Data Augmentation

To enhance the model’s robustness and generalizability, we applied a series of data augmentations to the training set. These included random horizontal and vertical flips, random 90-degree rotations, and a combination of shifting, scaling, and rotation with a scale limit of 0.3, a rotation limit of 15 degrees, and a shift limit of 0.1. Each augmentation was applied with a probability of 0.5.

Model Configuration and Implementation

Theoretically, our CL approach can be applied to any deep learning models. However, in our implementation, a Feature Pyramid Network (FPN) with a DenseNet-121 backbone, pre-trained on ImageNet, were used for both the teacher and the student models. The models were configured to accept 6-channel inputs (RGB, NIR, and SWIR) with a spatial dimension of 256×256 pixels. For the student model, which incorporates features from both coarse and fine data, the entire network was fine-tuned during training. During the 2nd stage, the teacher model was frozen to act as a stable knowledge source. All models were implemented using Python 3.9 and TensorFlow 2.13. The training and evaluation were conducted on a PC workstation with an Intel Xeon W-1350 CPU and an NVIDIA RTX A4000 GPU with 16GB of VRAM.

Training Parameters and Optimization

We employed the AdamW [Loshchilov and Hutter, 2019] optimizer, a variant of Adam that decouples weight decay from the gradient updates, with an initial learning rate of 1×10^{-3} and a weight decay of 1×10^{-4} . To manage the learning rate dynamically, we implemented a custom schedule that begins with a warm-up phase for the first 5 epochs, linearly increasing the learning rate to its base value. Following the warm-up, a ReduceLROnPlateau callback was activated, which reduces the learning rate by 0.5 if the validation Mean IoU (`val_Mean_IoU`) did not improve for 3 consecutive epochs. The models were trained for a maximum of 100 epochs with a batch size of 8. To prevent overfitting and ensure the retention of the best-performing model, we utilized an EarlyStopping callback that monitored the `val_Mean_IoU` with a patience of 10 epochs. The model weights that yielded the highest `val_Mean_IoU` on the validation set were saved and used for the final evaluation.

Baselines and Evaluation Metrics

We compare MineC2FNet against 2 groups of baselines: 1) CNN and Transformer-based models, and 2) CL-based methods. For the CNN and Transformer-based models, we trained FPN, DeepLabV3+, U-Net, and Prithvi (IBM-NASA geospatial foundation model) directly on our fine-grained dataset to establish a strong performance. For the CL-based methods, since no prior work addresses our coarse-to-fine CL domain adaptation task, we adapt LwF [Li and Hoiem, 2018], LwM [Dhar *et al.*, 2019], and Replay strategy [Rolnick *et al.*, 2019] such that the training involves transferring knowledge

Climate Zone (train/val/test)	Acc.	mF1	mIoU
Tropical (25/4/8)	95.19	86.44	67.63
Arid (63/4/21)	90.78	82.93	72.21
Temperate (24/4/9)	95.24	86.45	77.34
Cold (16/4/1)	85.82	72.99	57.47
Polar (11/4/2)	87.41	81.87	69.42

Table 11: Performance across Köppen-Geiger climate zones.

Metric	FPN	MineC2FNet (Ours)
mIoU	0.6825	0.7364 (+5.4)
Avg. Time (s)	0.0748	0.0909 (+0.0161)
Speed (FPS)	13.38	11.00 (-2.38)

Table 12: Model complexity and performance comparison between the baseline FPN and the proposed MineC2FNet.

from a teacher model (trained on coarse data) to a student model (trained on fine data). All models were trained using RGB, NIR, and SWIR bands as the input. Finally, we evaluate our framework and the baselines using standard semantic segmentation metrics: *Accuracy*, *Mean F1 Score* (for class imbalance), and *Mean Intersection over Union (mIoU)*.

7.4 Results and Discussion

Performance across Köppen-Geiger climate zones To assess the model robustness and the generalizability of its domain adaptation, we evaluated the model across five Köppen-Geiger climate zones [Beck *et al.*, 2018], covering a wide range of global climates, from tropical to polar. The results in Table 11 confirm MineC2FNet adaptability as it performs exceptionally well in arid and tropical zones, where mining activities are often concentrated, and achieves a peak mIoU of 77.34% in temperate climates. The performance in polar (69.42%) and cold (57.47%) zones, even with very limited data, proves that our domain-adapted model can effectively differentiate mining footprints across diverse geographic locations, including in underrepresented climate types and homogenous terrains.

Model Complexity and Efficiency

Finally, we evaluate the computational cost of our proposed MineC2FNet against the FPN baseline, with results presented in Table 12. The table clearly shows that MineC2FNet achieves a substantial performance gain, improving the mIoU by 5.4 points over the baseline.

This significant improvement in accuracy comes with a moderate trade-off in computational efficiency. Specifically, our model’s average inference time increased by 0.0161 seconds, resulting in a processing speed of 11.00 FPS compared to the baseline’s 13.38 FPS. This decrease in speed is an expected consequence of incorporating the more sophisticated selective continual learning mechanism (attentive feature injection and knowledge transfer). We argue that the considerable gain in segmentation accuracy justifies this modest increase in computational overhead for our remote sensing application, where model performance is often the primary consideration.

Configuration	Acc.(%)	F1(%)	mIoU(%)	Δ mIoU
BCE	0.9096	0.7733	0.6518	-
BCE+DICE	0.9016	0.7783	0.6545	+0.0027
BCE+DICE+SSIM	0.9039	0.7832	0.6642	+0.0124
BCE+DICE+SSIM+Bnd.	0.9102	0.7874	0.6687	+0.0169

Table 13: Ablation Study on Student Loss Components

Method	TN	FP	FN	TP (Mining)
MDIL-SS [Garg et al., 2022]	67.90	4.96	6.42	20.72
GSMF-RS-DIL [Huang et al., 2024]	69.63	5.89	5.28	19.20
MineC2FNet (Ours)	68.10	3.52	4.15	24.23

Table 14: Comparison of Confusion Matrix Results (%)

Impact of Student Loss Combinations

We conducted an ablation study to determine the optimal configuration for the student loss function, with a specific focus on enhancing edge delineation (see Table 13). While the baseline Binary Cross-Entropy (BCE) provides a foundation for pixel-wise classification, it struggles with structural integrity in fine-grained mining masks. The incremental addition of Dice and SSIM losses improved regional overlap and geometric shape preservation, respectively. Notably, the final inclusion of Boundary Loss yielded the highest performance (0.6687 mIoU) by weighting optimization toward edge pixels. This four-part combination effectively eliminates segmentation "blurring," ensuring the student model achieves the most precise delineation of mining site perimeters.

Confusion Matrix analysis

Based on our analysis of the confusion matrix (see Table 14), we provide quantitative evidence that MineC2FNet prioritizes foreground precision, a factor critical for high-fidelity environmental monitoring. While competing domain-incremental learning (DIL) methods, such as GSMF-RS-DIL, achieve high background classification accuracy, they exhibit higher False Positive Rates (FPR) and lower True Positive Rates (TPR) for the mining class. Specifically, MineC2FNet restricts the False Positive (FP) rate to 3.52%, marking a reduction of approximately 29–40% relative to MDIL-SS (4.96%) and GSMF-RS-DIL (5.89%). This transition from background-biased classification to foreground-focused precision directly accounts for the +2% IoU gap (see Table 1 in the main paper); by suppressing erroneous mining detections while simultaneously capturing more authentic mining footprints, MineC2FNet offers a more robust framework for tracking industrial expansion.